Investigation of the flow behaviour and local scour around single square-shaped cylinders at different positions in live-bed

Bordbar, Amir; Sharifi, Soroosh; Hemida, Hassan

DOI:
10.1016/j.oceaneng.2021.109772

Investigation of the Flow Behaviour and Local Scour around Single Square-Shaped cylinders at Different Positions in Live-Bed

Amir Bordbar*, [a]; Soroosh Sharifi [a]; Hassan Hemida [a]

[a] University of Birmingham (School of Engineering), Birmingham, UK (B15 2TT).

*Corresponding Author (Abordbar182@gmail.com)

Nomenclatures

S, S_{eq}	are the scour depth and equilibrium (quasi-equilibrium) scour depth $[L]$
w_p	is the cylinder's projected width $[L]$
U_∞	is the mean velocity of the undisturbed approach flow $[LT^{-1}]$
U_c	is the mean critical flow velocity for the initiation of motion for the bed materials $[LT^{-1}]$
U_x	is the streamwise velocity $[LT^{-1}]$
BF	is bluntness factor [-]
Fr	is Froude number [-]
u	is the ensemble average velocity $[LT^{-1}]$
t, T	are time $[T]$
ν	is molecular kinematic viscosity of the fluid $[L^2T^{-1}]$
u^+, y^+	are non-dimensional velocity and distance from the wall [-]
κ	is the von Karman's constant [-]
E	is a constant [-]
ΔB	is a function of dimensionless roughness height [-]
y	is the orthogonal distance of the centre of the first layer of cells from the wall $[L]$
C_μ	is a constant [-]
k	is turbulent kinematic energy per unit mass $[L^2T^{-2}]$
k_s	is bed Nikuradse equivalent roughness height [-]
${k_s}^+$	is the dimensionless (normalized) roughness height
C_s	is a roughness constant [-]
ω	is turbulence frequency or specific dissipation rate $[T^{-1}]$
n	is the normal vector of the wall or bed [-]
τ_b	is the skin friction shear stress $[ML^{-1}T^{-2}]$
T	is the deviatoric stress tensor $[ML^{-1}T^{-2}]$
c	is the local sediment volume concentration $[ML^{-3}]$
w_s	is the particle settling velocity $[LT^{-1}]$
D_Δ	is the deposition fluxes $[ML^{-2}T^{-1}]$
E_Δ	is the entrainment fluxes $[ML^{-2}T^{-1}]$

σ_c	is the concentration-dependent turbulent Schmidt number
c_e	is the equilibrium concentration at the reference level for entrainment [-]
c_b	is the concentration at the reference level for deposition [-]
θ	is Shields parameter [-]
θ_c	is critical Shields parameter [-]
$\theta_{c,0}$	is the critical Shields parameter for horizontal bed [-]
d_{50}	is the mean particle diameter $[L]$
d_*	is the dimensionless particle diameter [-]
Δ	is the reference level height from the bed $[L]$
u_f	is friction velocity (shear velocity) $[LT^{-1}]$
g	is acceleration of gravity $[LT^{-2}]$
s	is the relative density (specific gravity) [-]
c_D	is the drag coefficient for a particle [-]
D	is the circular cylinder diameter or squared-shaped cylinder side length $[L]$
h	is the mean flow depth $[L]$
δ	is the boundary layer thickness $[L]$
τ_∞	is the wall Shear stress of the undisturbed flow $[ML^{-1}T^{-2}]$
Q	is Q-criterion concept $[T^{-2}]$

Abstract. Scour around non-circular cylinders has seldom been studied before. This paper aims to numerically investigate the flow behaviour and evolution of local scour around two single square-shaped piers with 90° (square pier) and 45° (diamond pier) orientation angles to the flow under steady-current and live-bed conditions. For this purpose, a coupled approach between a hydrodynamic and a morphodynamic model is developed and validated against flow and scour experimental data sets. Hydrodynamic model simulations reveal the formation of strong horseshoe vortices (HSVs) upstream of the square pier compared to the diamond pier. The scour simulation results show a faster rate of increase in the scour depth around the square pier, which leads to a deeper equilibrium scour hole. The model gives values of normalized quasi-equilibrium scour depths of S_{eq}/w_p=1.94 and 1.00 for the square and diamond piers, respectively, where S_{eq} is the quasi-equilibrium scour depth, and w_p is the pier's projected width under steady current flow and live-bed conditions. It was discovered that the impact of other factors, such as bed material gradation, Froude number, Shields Parameter, as well as flow depth, can be as important as the shape factor in the study of equilibrium scour depth in live-bed conditions.

***Keywords**: Numerical Modelling, Scour, Sediment Transport, Square Pier, Flow Field Simulation*

1 Introduction

The presence of bottom-mounted obstructions, such as bridge piers and offshore wind turbine foundations in marine or riverine environments, changes the flow patterns in their vicinity and generates strong turbulent flow structures (Yagci et al., 2017; Kim et al., 2017; Sumer, 2002). These changes increase the local flow velocity and bed shear stresses near the structures and enhance the local sediment transport capacity in unprotected sea or riverbed conditions. This leads to the erosion of the seabed or riverbed around structures, a phenomenon that is termed local scour (Zhang et al., 2017). Local scour lessens the insertion depth of the structure's foundation and weakening its bearing capacity causing structural failure and financial or life loss (Wang, 2020; Mahmoud, 2020).

The spectrum of factors that influence the development of scour around marine and riverine foundations brings a high level of uncertainty into the design of a safe and economically viable hydraulic structure (Akhlaghi et al., 2020; Mir et al., 2019; Mir et al., 2018; Miyab et al., 2017). In the case of a single cylinder (e.g., monopile, single pier), one of these influencing factors is cross-section geometry. Under a defined approaching flow and bed material conditions, the cross-section geometry controls the flow and scour pattern in its vicinity (Mir et al., 2019).

Over the past few decades, the flow behaviour and local scour around circular cylinders have been widely studied, both numerically and experimentally. The works of Vaghefi et al. (2018), Schendel et al. (2018), Qi et al. (2019), Zhang et al. (2017), Pan et al. (2020), Pandey et al. (2020) and Nagel et al. (2020) can be mentioned as more recent and noticeable studies in this group. Nevertheless, studies on non-circular cylinders are quite confined in the pertinent literature. Physical modelling of scour development around square-shaped cylinders can be found in the works of Sumer et al. (1993), Diab et al. (2010), Yao et al. (2018) and Omara et al. (2020). Ismael et al. (2015) experimentally studied scour around an egg-shaped pier with different orientation angles to the flow. Al-Shukur et al. (2016) and Mir et al. (2018) experimentally investigated the impact of several different pier shapes (circular, rectangular, octagonal, chamfered, hexagonal, elliptical, sharp, Joukowsky, oblong, streamline and rounded) on the development of local scour. While these studies appreciated the importance of the piers' cross-section shape on the evolution of local scour patterns, they proposed different equations for the prediction of scour development based on the changes in the cross-section shapes.

A few studies on numerical modelling of scour around non-circular cylinders have also been reported in the literature. In the majority of these studies, the modelling of scour has been achieved by coupling a hydrodynamic model with a morphodynamic model. This approach is hereafter referred to as the classical approach. In this approach, the erosion of a sandy bed is obtained by solving a mass-balance equation over the bed owing to sediment transport models results. This approach has been successfully employed in simulation of local scour around circular piles in different studies (e.g., Baykal et al., 2017; Liu and García, 2008; and Stahlmann and Schlurmann, 2012), but its performance on the prediction of local scour around non-circular piers has been rather controversial. Abbasnia and Ghiassi (2011) and Ghiassi and Abbasnia (2013) used the classical approach to simulate the local scour around circular, square and rectangular piers in clear-water conditions. The Unsteady Reynolds Averaged Navier-Stokes (URANS) equations in combination with the k-ε turbulence model was applied to solve the flow field. The morphodynamic part of their model included both bedload and suspended load models using the approaches proposed by Rijn (1984a) and Rijn (1984b), respectively. They considered the effect of vorticity in the calculation of the bed shear stress to improve the performance of their model. However, no validation against the hydrodynamic parameters was provided, their model results matched well with their empirical data on scour around square pier. In another study, Khosronejad et al. (2012) studied both experimentally and numerically the scour around circular, square, and diamond bridge piers in clear-water conditions. In their scour simulation model, the URANS equations closed with the k-ω turbulence model was applied to simulate the flow field, and the morphodynamic part contained a bedload model, as described in Khosronejad et al. (2011). They reported that the accuracy of their scour model depended on the piers' cross-section shape. Khosronejad's model lacked accuracy in capturing the dynamics of the HSV system and predicting local scour around square and circular piers. In a more recent study, Omara et al. (2019) used FLOW-3D to numerically estimate the flow behaviour and scour depth around vertical and inclined bridge piers. They applied the renormalization group (RNG) k-ε turbulence model to solve turbulent stresses in URANS equations, while their sediment transport model included both bedload and suspended load. They pointed out that the prediction capability of the model was attached to the pier's shape and inclined direction.

As noted above, only a limited number of studies on scour around non-circular cylinders exist. Most of these studies investigated scour in clear-water conditions, where the mean velocity of the undisturbed approaching flow, U_∞, is less than the mean critical flow velocity for the initiation of motion of bed materials, U_c. On the contrary, there is very limited information available on scouring under live-bed conditions where $U_\infty > U_c$. The mechanism of scour under live-bed conditions is quite different from clear-water conditions (Najafzadeh et al., 2014). Hence, for the first time, the present study aims to numerically investigate the impact of pier cross-section geometry with respect to the flow on the local scour under live-bed conditions around square-shaped piers to add to the knowledge of scour mechanism around non-circular piers.

The results of previously developed models on the study of non-circular cylinders, specifically Khosronejad et al. (2012) and Omara et al. (2019), demonstrated the drawback of the models in the prediction of scour around piers with different cross-section shapes. Hence, a new and improved model based on the classical approach was developed in the OpenFOAM® framework. In this model, the *k-ω SST* turbulence closure model, which has proven capability in predicting adverse pressure gradients and separation flow, is employed to solve the Reynolds stress terms in the URANS equations (Menter, 1992). This combination was chosen to ensure a precise prediction of the formation of HSV and lee-wake vortices around the piers. On the other hand, the model includes both bedload and suspended load sediment transport modes, while proper attention is given to the position of the splitting layer (reference layer) between these two transport modes.

The model is validated against the experimental data for flow behaviour and bed shear stress distribution around circular cylinders by Dargahi (1987) and Melville (1975) and scour prediction around circular and square-shaped piers by Roulund et al. (2005) and Khosronejad et al. (2012). The results confirm that the capability of the model in reproducing the results was almost independent of the pier's cross-section shapes.

The mathematics of the model is briefly described in the next section. In section 3, the results of the validation of the model are provided. In section 4, the model's results in prediction of the flow behaviour on a rigid flat bed and scour development in live-bed conditions around a square-shaped pier with 45° and 90° orientation angle to the flow are presented. Additionally, the robustness and reliability of the model in simulations are evaluated based on the available data from the literature. Finally, in the conclusion section, the findings and main contributions of this work are summarised and discussed.

2 Coupled hydro-morphodynamic model

2.1 Hydrodynamic model

The developed model in this study is based on the classical approach. The hydrodynamic part of the model only solves the water phase around the piles. Hence, in all cases, the computational domain is limited to the water-air interface on top. This is a valid assumption for almost all practical cases while the ratio of the inertial force to gravitational force, Froude number (Fr), is small (e.g., Fr < 0.2) in the flow (Roulund et al., 2005). The hydrodynamic part of the model solves continuity and URANS equations for a single-phase incompressible flow. This system of equations is closed by using the two-component turbulence model *k-ω SST* to solve the Reynolds stress terms as it is implemented in OpenFOAM®.

The flow and turbulent properties need to be quantified at the boundaries of the computational domain. In all investigated cases in this study, the boundaries are top, bed (rough wall), inlet, outlet, sides and pier body (smooth wall), as shown in Figure (1). In the near-wall region, the physics of the flow is expressed by adapting a simple near-wall treatment proposed by Cebeci and Bradshaw (1977), which is valid for the logarithmic region of the boundary layer. Based on this approach, where the roughness of the surface is known, the near-wall treatment for the logarithmic region of the boundary layer is defined by:

$$u^+ = \frac{1}{\kappa}\ln(Ey^+) - \Delta B \qquad (1)$$

$$y^+ = y\frac{C_\mu^{1/4}k^{1/2}}{\nu} \qquad (2)$$

where $u^+$and $y^+$are non-dimensional velocity and distance for the log-low region in the equilibrium turbulent boundary layer, respectively, E is a constant equal to 9.8, $\kappa = 0.4$ is the von Karman constant, C_μ is a constant equal to 0.09, k is turbulence kinetic energy, y is the orthogonal distance of the centre of the first layer of cells from the wall and ν is the kinematic viscosity of the fluid. ΔB in Eq. (1) depends on the dimensionless (normalized) roughness height k_s^+:

$$k_s^+ = \frac{k_s c_\mu^{1/4} k^{1/2}}{\nu}, \tag{3}$$

where k_s is bed Nikuradse equivalent sand roughness height. Cebeci and Bradshaw (1977) provide three different regimes for the calculation of ΔB based on k_s^+ as follows:

$$\Delta B = \begin{cases} 0, & k_s^+ < 2.25 \\ \frac{1}{\kappa}\ln\left[\frac{k_s^+ - 2.25}{87.75} + C_s k_s^+\right] sin[0.4258\,(ln\,k_s^+ - 0.811)], & 2.25 \le k_s^+ \le 90 \\ \frac{1}{\kappa}\ln[1 + C_s k_s^+], & k_s^+ > 90 \end{cases} \tag{4}$$

where C_s=0.6 is the roughness constant. In this work, all the walls, including the rough sandy bed and smooth pier body, are treated with Cebeci and Bradshaw's (1977) near-wall treatment. For both smooth and rough walls, the turbulence kinematic energy near the wall is treated by the Neumann condition (zero normal gradient), and turbulent frequency, ω, is calculated following Ferziger and Peric's (2008) model, which is valid for the logarithmic region of the boundary layer:

$$\omega = \frac{\sqrt{k}}{C_\mu^{0.25} \kappa y}. \tag{5}$$

The velocity is determined with a no-slip condition ($\vec{u} = 0$), and pressure is set as zero normal gradient condition at the walls. The sides are satisfied with symmetry boundary condition for all quantities. Replacing the flume side walls with a symmetry boundary condition at the sides of the computational domain is a justifiable assumption, as the effect of the flume width on the approaching flow was negligible. In all cases, the computational domain width was considered wide enough (~10D to 20D for different test cases while D is the circular cylinder diameter or square-shaped cylinder side length) to ensure the impacts from the side boundary condition are minimum. At the top, the water-air interface is modelled with a plain surface with a slip boundary condition. At the inlet, the velocity vectors and turbulent quantities are supplied by following the Dirichlet condition. The pressure is treated with the Neumann (zero normal gradient) condition. Finally, the outlet is treated with zero values for the gradient of all quantities except for the pressure, where a Dirichlet condition with a value equal to zero is imposed.

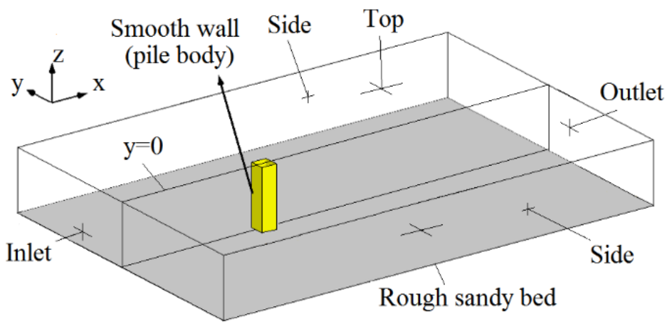

Fig. 1 boundaries of the computational domain

2.2 Bed shear stress

Computed bed shear stress from the flow field results serves as the primary input parameter to the sediment transport models. Hence, a precise calculation of the bed shear stress is essential to achieve realistic sediment transport results. In this model, the shear stress acting on the bed ($\boldsymbol{\tau_b}$) is gained from:

$$\boldsymbol{\tau_b} = \boldsymbol{T}.\boldsymbol{n} \qquad (6)$$

where $\boldsymbol{n}$ is the unit normal vector of the bed face, and $\boldsymbol{T}$ is the deviatoric stress tensor.

2.3 Morphodynamic model

The sediment transport model used in this work contains both bedload and suspended load. The bedload model computes the flux of the sediments that roll, slide or jump along the bed in a thin layer very close to the bed. For sediments transported above the bedload layer, the suspended load model calculates the sediment flux. These two sediment transport modes are separated by a hypothetical layer called reference level. An extension of the empirical equation proposed by Engelund and Fredsøe (1976) for 3D cases is applied for the bedload model, while the suspended load is considered by employing an advection-diffusion equation, as follows:

$$\frac{\partial c}{\partial t} + \nabla.[(\boldsymbol{u} + \boldsymbol{w_s})c] = \nabla.\left[\left(\vartheta + \frac{\vartheta_t}{\sigma_c}\right)\nabla c\right] + E_\Delta - D_\Delta \tag{7}$$

where c is the volumetric (dimensionless) suspended sediment concentration, t is time, $\boldsymbol{u}$ and $\boldsymbol{w_s}$ are the fluid velocity and sediment fall velocity vectors, respectively. The fall velocity is calculated using the method proposed by Soulsby (1997). $\vartheta + \vartheta_t/\sigma_c$ is the sediment diffusivity coefficient, where σ_c is the concentration-dependent turbulent Schmidt number, which is chosen as 0.8, similar to Liang and Cheng (2005). The terms of E_Δ and D_Δ in the right hand-side of Eq. (7) determine the quantities of the total flux from the bed into the suspended load mode (entrainment) and vice versa (deposition), respectively. An approach used by Warner et al. (2008) and Stahlmann (2013) is followed to consider the exchange of particles in the advection-diffusion equation. The entrainment rate is obtained from:

$$E_\Delta = c_e w_s \tag{8}$$

where c_e is the equilibrium (reference) concentration of suspended load at the reference level height from the bed Δ. c_e can be obtained from Rijn (1984b):

$$c_e = 0.015 \frac{d_{50}\left(\frac{\theta - \theta_c}{\theta_c}\right)^{1.5}}{d_*^{0.3}\Delta} \tag{9}$$

where θ is the Shields parameter:

$$\theta = \frac{u_f^2}{g(s-1)d} \tag{10}$$

where u_f is the friction velocity, g is the acceleration of gravity, s is the relative density of the sand and d is the grain diameter. In Eq. (9), θ_c is the critical Shields parameter corresponding to the initiation of the sand particles motion and d_* is the non-dimensional grain size:

$$d_* = \left[\frac{g(s-1)}{\vartheta^2}\right]^{1/3} d_{50} \tag{11}$$

where d_{50} is the mean grain diameter.

Applying Eq. (9), Rijn (1984b) proposed Δ equal to half of the bed-form height or sand roughness height, while the minimum Δ is 0.01 of the water depth. Liang and Cheng (2005) proposed $\Delta=3.6d_{50}$ as an acceptable value in 2D numerical modelling of scour below a submarine pipeline. In the present work, the height of the centre of the first layer of cells closest to the bed, which corresponds to the reference level, is considered equal to $4d_{50}$ in all simulations. With good approximation, this reference level (the first layer of grids above the bed) is located in the logarithmic region of the boundary layer (Refer to Driest (1956)), which satisfies the applied near-wall treatment requirements, as well.

The deposition rate, D_Δ, is obtained from the approach suggested by Liu and García (2008):

$$D_\Delta = c_b w_s \tag{12}$$

where c_b is the sediment concentration at the reference level, which here, is equal to the sediment concentration at the centre of the first layer of cells closest to the bed.

Finally, the results of the sediment transport model are reflected by solving a mass-balance equation (Exner, 1925) over a 2D mesh, corresponding to the bed boundary of the 3D computational domain. In addition, a sand sliding method was also followed to avoid unreal bed slopes. Bordbar et al. (2021) investigated two different sand sliding techniques, namely, Artificial Transport Rate Method (ATRM) by Roulund et al. (2005) and Geometry-Based Method (GBM) by Jacobsen (2015). It was realized that ATRM offers a solution with a considerably lower numerical error in comparison to GBM. Therefore, in the present study, a similar method to ATRM is used.

3 Validation

The hydrodynamic part of the model was validated against data from Dargahi (1987) and Melville (1975), who studied flow behaviour and bed shear stress distribution around circular piles mounted on sand-covered flat plates, respectively. The investigation was limited to circular pile cases, as investigation of flow behaviour and bed shear stress distribution around non-circular piles has been rarely done (e.g., Hjorth, 1975), and the authors could not find any reliable data sets for model validation. On the other hand, the performance of the hydro-morphodynamic model on the prediction of scour evolution around piers with different cross-section shapes was evaluated against the measurements reported by Roulund et al. (2005) and Khosronejad et al. (2012) for circular and square-shaped cylinders, respectively. The specifications of the experimental tests are provided in Table 1.

Table 1. Relevant Information on Experimental Conditions Modelled in the Present Study

Experiment	Dargahi (1987)	Melville (1975)	Roulund et al. (2005)	Khosronejad et al. (2012) (square)	Khosronejad et al. (2012) (diamond)
Bed condition	Flat -Rigid	Flat-Rigid	Mobile	Mobile	Mobile
Flume dimensions (length/width) (m)	22 / 1.5	19 / 0.456	10 / 4	10 / 1.21	10 / 1.21
pier width perpendicular to the flow direction w_p (m)	0.15	0.051	0.1	0.165	0.2335
Pier distance from the inlet (m)	-	-	6.6	4	4
Mean particle diameter d_{50}(mm)	0.36	0.385	0.26	0.85	0.85
Mean flow velocity U (m/s)	0.26	0.25	0.46	0.22	0.21
Mean flow depth h (m)	0.2	0.15	0.4	0.139	0.157
Boundary layer thickness δ (m)	-	-	0.2	-	-
Froude number $Fr=U/(gh)^{0.5}$	0.19	0.21	0.23	0.19	0.17
Bed Nikuradse equivalent sand roughness k_s (mm)	0.9	0.96	0.65	2.55	2.55
Critical Shields Parameter for horizontal bed θ_{c0}	-	-	0.05	0.03	0.03

3.1 Flow field and bed shear stress

3.1.1 Flow Field around a circular cylinder

Dargahi (1987) carried out a set of measurements to study flow velocity around a circular cylinder. The experimental data included the vertical distribution of streamwise velocity, U_x, at five different distances upstream and downstream of the cylinder on the symmetry plane. The numerical setup for the test included a computational domain 3 m long, 2 m wide and 0.2 m high, i.e., equal to water depth. The generated mesh included around 500,000 grids. The height of the centre of the first layer of mesh closest to the bed was equal to 1.5 mm ($\sim 4d_{50}$) to ensure that the requirement of the applied near-wall treatment, given by Cebeci and Bradshaw (1977), is satisfied. The fully-developed flow was set for the inlet, while the other boundaries were treated, as described in section 2.

The simulations results were also compared with the modelling results of Salaheldin et al. (2004) and Omara et al. (2019), who used the same data sets from Dargahi (1987). Salaheldin et al. (2004) applied the URANS equations in combination with several variants of the k-ε model (e.g., k-ε standard, k-ε RNG, k-ε realizable) and the Reynolds Stress Model (RSM). They found that the RMS model provided the most satisfactory results. Omara et al. (2019) applied the k-ε RNG model as it was implemented in FLOW 3D and have made the comparison only for the upstream of the pier.

The results from the present study, reported empirical data by Dargahi (1987), simulation results of Salaheldin et al. (2004) for the RSM model and Omara et al. (2019) are presented in Figure (2), and the Root Mean Square Errors (RMSE) for the simulation results against the experimental data are provided in Table 2. It is observed that the result of the present study shows very good agreement with the experimental data. The accuracy of the results indicates that the modelling of the water-air interface at the top of the computational domain with slip boundary condition is an acceptable assumption in low Froude numbers. On the other hand, the present model predicted a reverse flow at x/D= -0.73 and the area very close to the bed due to the formation of an HSV upstream of the pier. This pattern was not reported in the experimental data, which can be due to the lack of accurate measurements in Dargahi's investigation.

Table 2. the results of RMSE for simulations against the measurements data by Dargahi (1987)

x/D	-2.5	-0.73	0.57	2.1	8.0
Present Model	0.0074	0.0049	0.0308	0.0191	0.0074
Salaheldin et al. (2004) RSM model	0.0060	0.0067	0.0550	0.0132	0.0133
Omara et al. (2019)	0.0176	0.0051	-	-	-

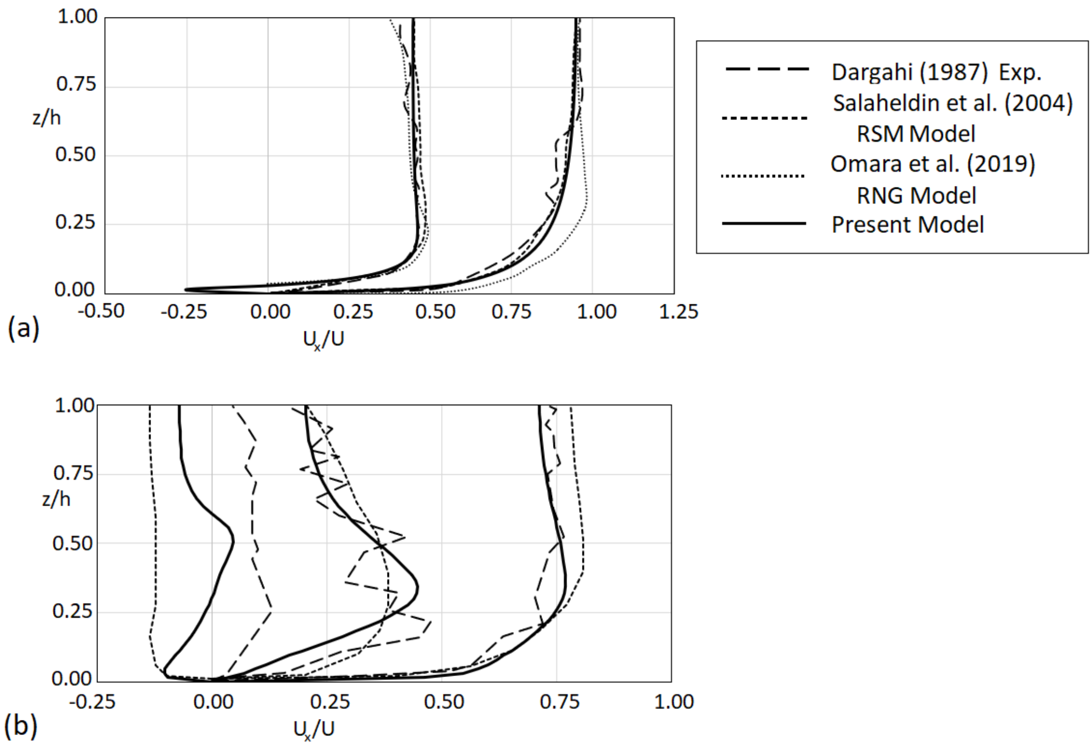

Fig.2 comparison between the modelled streamwise velocity U_x at the plane of symmetry (a) upstream (b) downstream of the pier.

3.1.2 Bed shear stress distribution around a circular cylinder

Melville (1975) reported the distribution of the normalized local bed shear stress around a circular cylinder, as reported in Table 1. To evaluate the performance of the present hydrodynamic model, the experiment was numerically reproduced. The numerical setup for the test included a computational domain 2 m long, 1 m wide and 0.15 m high, i.e., equal to water depth. The generated mesh included around 400,000 grids. The height of the centre of the first layer of mesh closest to the bed was equal to 1.5 mm ($\sim 4d_{50}$). A fully-developed flow condition was set for the inlet, while the other boundaries were treated as described in section 2.

Figure (3) illustrates Melville's (1975) measurement results and Mendoza-Cabrales's (1993) simulation results for the test case on top and the results of the present model on the bottom. The results of the present model agree very well with the reported experimental data in terms of prediction of the location of the maximum shear stress; however, both numerical models overestimate the magnitude of the maximum shear stress.

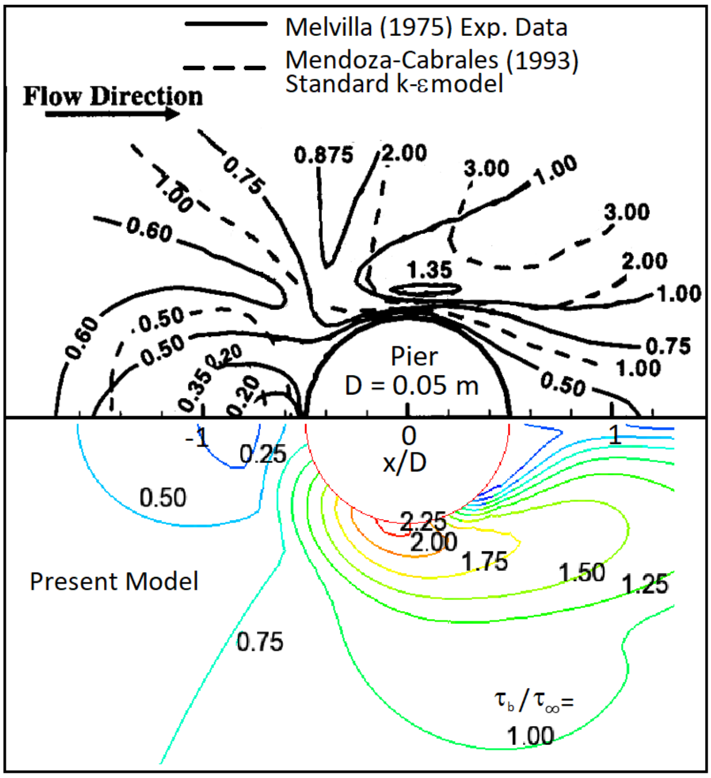

Fig.3 (top) reported normalized bed shear stress distribution on flat bed by Melville (1975) and simulation results by Mendoza-Cabrales (1993); (bottom) present model simulation result.

3.2 Local scour

3.2.1 Local scour around a circular pier in live-bed

The performance of the developed hydro-morphodynamic model was evaluated against experimental data from Roulund et al. (2005) for scouring around a circular pile in live-bed conditions. The details of the experimental conditions can be found in Table 1.

The numerical setup for the test included a computational domain 3 m long, 2 m wide and 0.4 m high, i.e., equal to water depth. A pile with 0.1 m diameter was considered at 1 m downstream of the inlet boundary. The boundaries were treated as described in section 2. The height of the centre of the first layer of cells nearest to the bed was set equal to 1 mm ($\sim 4d_{50}$). This value was chosen to assure that the centre of the first layer of mesh closest to the bed was placed in the log-layer region of the boundary layer while also satisfying the requirement of the reference level height from the bed. The inlet velocity was obtained by fitting a curve to the data provided in Roulund et al. (2005).

As the hydro-morphodynamic model simulations are very time-consuming, a mesh independency study was carried out for only the first 30 s of the physical time where a coarse mesh with around 400,000 grids and a fine mesh with around 600,000 grids were compared. This short time period included very rapid changes in the bed morphology, as the scour hole depth after the first 30 s was more than one-fifth of the equilibrium scour depth reported by Roulund et al. (2005). Therefore, this time period was assumed long enough to study mesh independency. The topography of scoured bed for both meshes is provided in Figure (4). The results are quite similar in the area adjacent to the pier. Some discrepancy can be observed downstream of the pier, which can be justified by understanding the stochastic nature of the sand sliding mechanism. As a result, the coarse mesh was chosen for the full-time modelling. The simulation was run for T=1 hour of physical test and took around three and a half months on a 2.3 GHz CPU with 8 GB RAM.

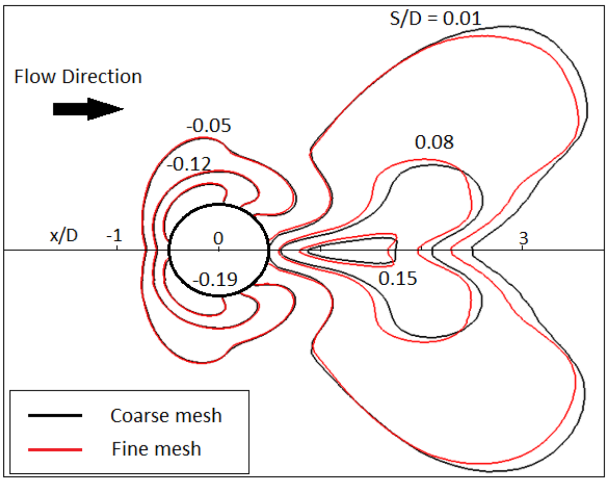

Fig.4 mesh independency study results for simulation of local scour around a circular pier

Figure (5) displays the results of the empirical measurements from Roulund et al. (2005) in comparison with the simulation results from Roulund et al. (2005), Gothel (2008), Stahlmann (2013) and the present model in terms of the evolution of the scour hole depth at the upstream and downstream edge of the circular pile. The dimensionless number S/w_p presents the ratio of the scour depth S to the pile width w_p. The RMSE of the simulations against the measurements is presented in Table 3. It can be seen that the present model outperforms the other three numerical models at the upstream edge. The present model follows the trend of the experimental data with the least deviation where experimental data existed in comparison to all the other simulations (as shown in Table 3). The results for the downstream edge were only available from Roulund et al. (2005). The present model overestimated the scour depth at the downstream edge from early-stage and displayed a discrepancy of around 18% from the empirical data after 1 hour. It is to be noted that the present model predicted the maximum scour depth occurrence to be at the sides of the pile with S/w_p= 1.25.

Table 3. RMSE of simulations against Roulund et al. (2005) experimental data

Measurement	Present Model	Roulund et al. (2005)	Gothel (2008)	Stahlmann (2013)
Upstream	0.0449	0.1052	0.2177	0.0475
Downstream	0.1150	0.0880	-	-

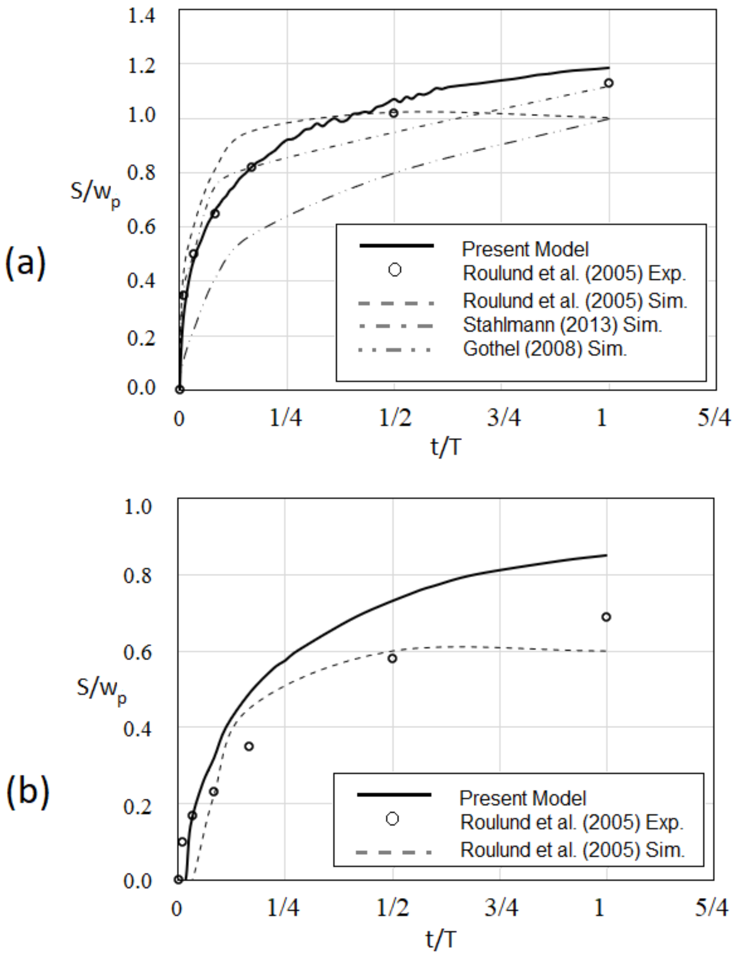

Fig. 5 temporal scour hole depth at (a) the upstream and (b) downstream edge of the circular pile

3.2.2 Local scour around a square and diamond pier in clear-water

The intensity of the mean HSV forming upstream of mounted piers is one of the main factors in developing the local scour, which depends on the mounted pier nose geometry (Khosronejad et al., 2012). Fleming et al. (1993) addressed the pier nose geometry with a character named bluntness factor (BF). Piers with larger BF face stronger HSVs. To evaluate the robustness of the model on the evolution of scour hole around piers with different cross-section shapes, the model was verified against experimental cases of square and diamond piers, reported by Khosronejad et al. (2012) as corresponding to $BF \rightarrow \infty$ and 0, respectively.

Two sets of experiments for a square-shaped pier with a side length of 16.51 cm with 90° (square pier) and 45° (diamond pier) orientation angles to the flow were considered for model assessment. More details of the tests are shown in Table 1. Both tests were carried out under clear-water conditions.

The numerical simulation for both cases was followed in computational domains 3 m long and 2 m wide where the piers were located 1 m downstream of the inlet. The height of the domain was set equal to the water depth in each case. A mesh dependency test was also done for these cases, and 3D meshes with around 380,000 grids were chosen for full-time modelling. The approaching flow attributes at the inlet were supplied by a preliminary hydrodynamic simulation, which was conducted for a domain with the same condition as the original mesh and with 3 m length. The length was considered 3 m to provide the approaching flow with the same condition as the experiment. The other boundaries were treated as described in section 2. The critical Shields parameter value for horizontal bed, $\theta_{c,0}$, in this test was calculated from the equation proposed by Soulsby and Whitehouse (1997):

$$\theta_{c0} = \frac{0.3}{1 + 1.2d_*} + 0.055\left(1 - e^{-0.02d_*}\right). \tag{13}$$

Figure (6) demonstrates the time evolution of maximum scour depth for T=1 hour of physical modelling for both diamond and square piers. The simulations are compared against the experimental measurements using the RMSE in Table 4. In the case of the square pier, the result from the present model outperforms Khosronejad et al.'s (2012) numerical model, while both simulation results underestimated the scour progression. Khosronejad et al. (2012) did not provide the value of the critical Shields parameter for the initiation of sand motion. Therefore, as mentioned above, the value was estimated using the proposed equation by Soulsby and Whitehouse (1997). This can be why there's a difference between the present simulation and experimental results. Nevertheless, the numerical results for diamond pier are roughly similar. In the equilibrium condition for the present model, the differences of 6.7% and 13.1% from the experimental measurements are observed for the square and diamond pier cases, respectively.

Table 4. RMSE of simulations against Khosronejad et al. (2012) experimental data

Measurement	Present Model	Khosronejad et al. (2012)
Square pier	0.0221	0.0843
Diamond pier	0.0469	0.0312

Figure (7) illustrates a comparison between the topography of the scoured bed from the simulation and the laboratory measurements from Khosronejad et al. (2012) for the diamond and square piers. The experimental results are only provided for one side of the symmetry plane y=0 in Khosronejad et al. (2012). The simulation results are almost symmetric with respect to the plane y=0. In the square pier case, as a result of laboratory measurements, Khosronejad et al. (2012) mentioned that the maximum scour depth happened in the front corners of the pier, while the area with significant depth was observed around the nose of the pier. The present numerical model also found the maximum scour depth in the front corners of the pier; however, it failed to accurately predict the depth of the scoured area around the front side of the pier. In contrast, the maximum deposition height position given by the numerical model agrees with experimental measurements. For the diamond pier, a good agreement in the position of the maximum scour depth and deposition height is observed between the numerical simulation results and experimental data. The obtained results from the simulations indicated that the present model has a good capability in the prediction of main characteristics of scour around piers with different cross-section shapes. Therefore, the model was applied to investigate scour around square-shaped piers in live-bed conditions.

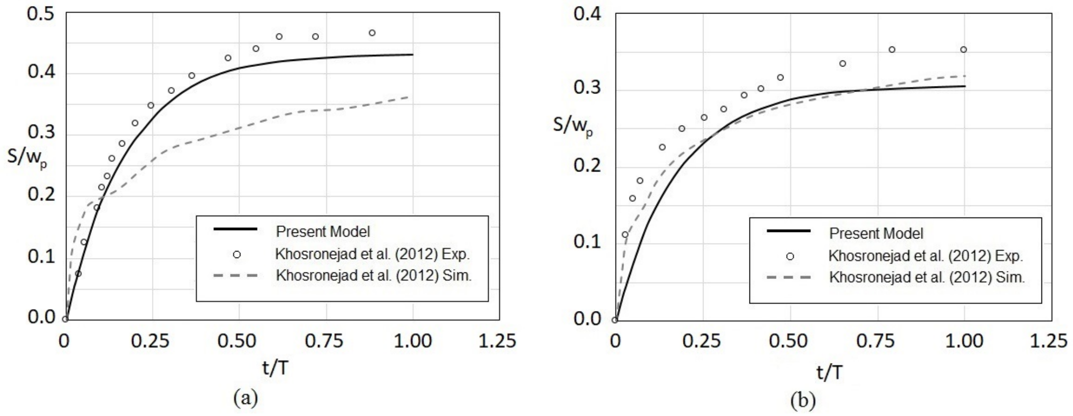

Fig. 6 changes in scour depth with time in case of (a) the square and (b) diamond pier

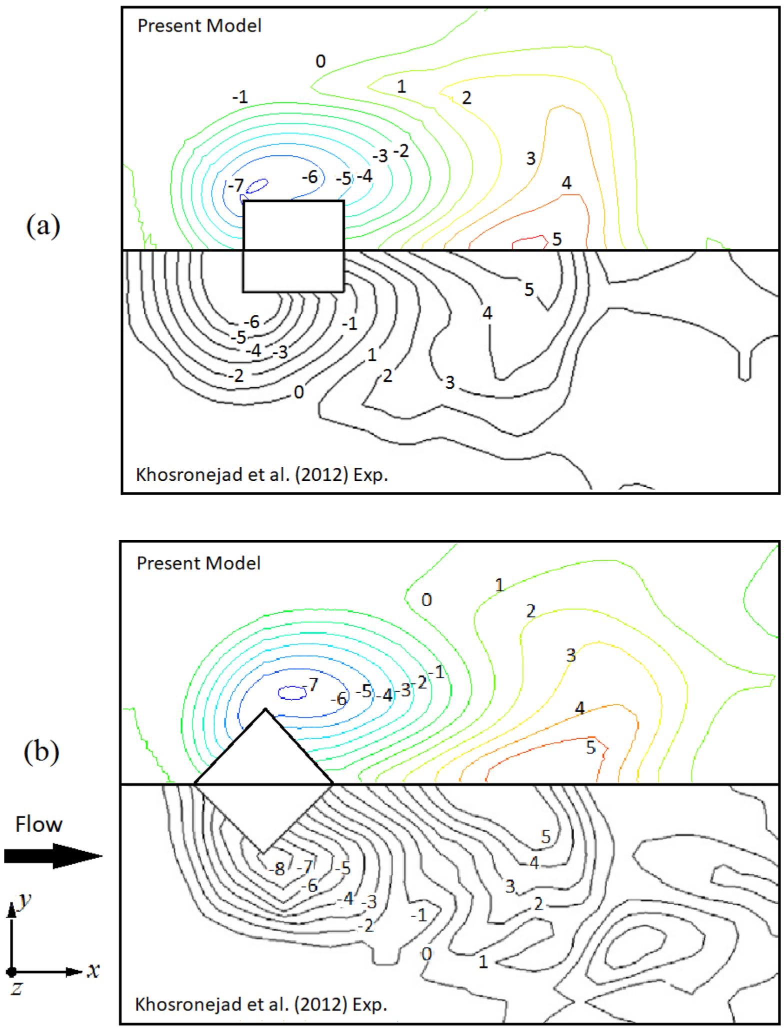

Fig. 7 Comparison of simulated (top) and measured (bottom) bed topography at equilibrium condition for (a) square pier, (b) diamond pier (The measurement unit is cm).

4 Results and Discussion

4.1 Live-bed simulations model setup

In this section, the developed and validated model is employed to numerically investigate the effect of pier geometry on flow behaviour and scour in live-bed conditions. For this purpose, a similar setup to the circular pile of Roulund et al. (2005) in Table 1 was applied for diamond and square piers test cases. Numerical simulations were done for a square-shaped pier with a side length of D=10 cm, which meant the pier width in the flow direction was 10 and 14.1 cm in the cases of the square and diamond pier, respectively. Computational meshes with similar dimensions and boundary conditions used for modelling the circular cylinder test case were considered, and the piers were placed 1 m downstream of the inlet. Two sets of numerical simulations were run. First, to investigate the flow field around the piers, the hydrodynamic model was solved on a rough rigid bed condition for each case. Next, the coupled hydro-morphodynamic model was employed to simulate the local scour development in the vicinity of the piers in the mobile sandy bed. The same generated meshes were used in both series of tests. Meshes with around 400,000 grids were chosen.

4.2 Flow field simulations on a rigid bed

To study the flow field in the vicinity of the piers, the hydrodynamic model was solved for both square and diamond piers mounted on a rigid flat sandy bed. Figure (8) illustrates the formation of HSV and lee-wake shed vortices upstream and downstream of the piers in URANS simulations using the iso-surfaces technique for the Q-criterion concept (Hunt et al., 1988). The Q-criterion concept demonstrates a vortex as a “connected fluid region with a positive second invariant of ∇u” (Kolář, 2007). It is observed that the separated flows start to form on the front and side corners of the square and diamond piers, respectively, which are responsible for producing the reverse-vortex flows and quasi-periodic vortex shedding downstream of the piers. It is also seen that the behaviour of the HSVs upstream of the piers is almost independent of the quasi-periodic motion of the shed vortices, while the elongated part of the HSVs downstream of the piers can be affected by the shed vortices.

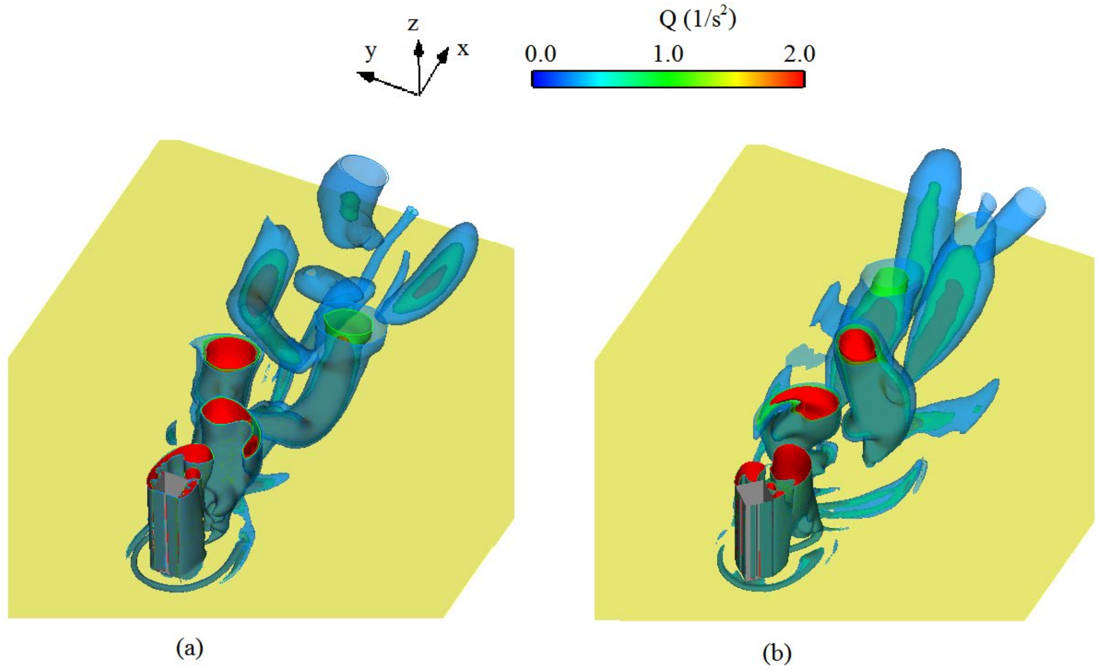

Fig. 8 turbulence structures around (a) square and (b) diamond piers using the Q-criterion concept

Figure (9) illustrates the traced streamlines over the mean flow fields at symmetry plane y=0 upstream of the piers. Due to the impact of the square pier nose, a strong down-flow is formed upstream of the pier. The formation of two HSVs is predicted upstream of the square pier, which includes one main vortex rotating in the clockwise direction and one smaller vortex rotating in the counter-clockwise direction and very close to the pier body. In the case of the diamond pier, a very weak down-flow is observed upstream of the pier nose. As a result, the predicted HSV system comprises only one small vortex upstream of the pier in comparison to that of the square pier.

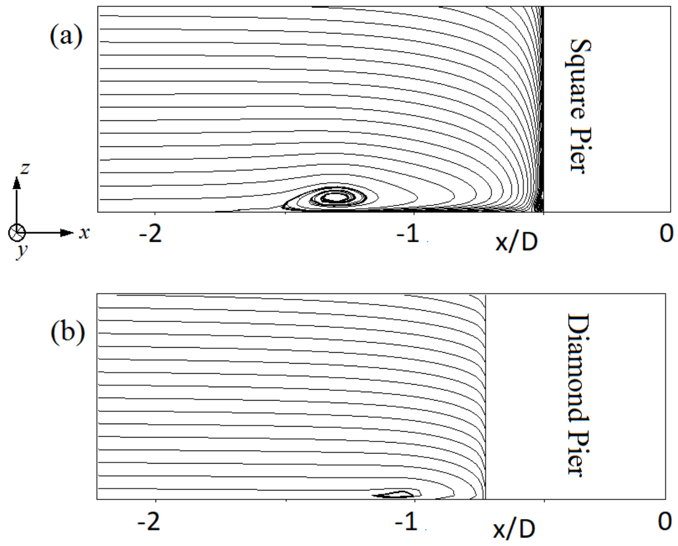

Fig. 9 formation of HSVs upstream of (a) square pier and (b) diamond pier.

4.3 Scour simulations on a mobile bed

The coupled hydro-morphodynamic model was employed to study local scour on a mobile bed. In these simulations, the bottom boundary of the domains was set as a mobile bed. The models were run for T= 1 hr of physical tests, as it was assumed that the quasi-equilibrium condition is obtained for all cases within the first one hour. Figure (10) displays the topography of the scoured bed at times t/T = 0.0083, 0.0333, 0.25, 1 from the start of the simulation for both square and diamond piers. In both cases, it is observed that scouring started from the early stages of the simulation and extended in terms of the maximum depth and the affected area. In both cases, the maximum scour depth happens on the sides of the piers. As expected, stronger scouring occurred around the square pier, corresponding to the remarkably stronger HSVs, while for the diamond pier, scouring is more likely due to the local acceleration of flow velocity around the pier. Observing the morphology of the bed over time shows that some asymmetry may arise downstream of the piers. This dissimilarity, which is in accordance with the nature of scouring, can be explained with the stochastic nature of quasi-periodic lee-wake vortices along with the nature of sand sliding.

Figure (11) presents the instantaneous flow field at plane y=0 upstream of the piers in the quasi-equilibrium scour depth condition. The instantaneous flow velocity vector field is used to visualize the development of the HSV upstream of the piers. It is observed that the presence of the square pier produces a strong adverse pressure gradient upstream of the pier leading to the formation of HSV, which spreads over the entire scour hole upstream of the pier. On the other hand, in the case of the diamond pier, the formed HSV is small and feeble, with a low impact on the progression of scouring.

To better understand the morphology of the deformed bed in quasi-equilibrium conditions, the corresponding contour of bed displacement around the circular, square and diamond piers is displayed in Figure (12). It is observed that for the square pier, the area with maximum scour depth is wrapped around the entire front side of the pier, while in the case of the diamond pier, this area is attached to the side corners, and in the case of the circular pier, it occurs in a radial angle at around 70° from the head. It is also noticed that a wider area around the square pier is affected by scouring in comparison with the two other cases. This is a rational consequence of the formation of a deeper scour hole around the square pier.

Figure (13) shows the progress of normalized local scour depth S/w_p around the circular, square and diamond piers during the first one hour of scouring. It is observed that the rate of increase in scour depth reduces in time for all cases. For the entire simulation, the rate of increase in scour depth around the square pier is faster than the diamond and circular pier, which leads to a deeper scour hole after one hour. On the other hand, the evolution process for all cases is progressed with rather similar speed. The maximum scour depth after one hour of scouring for circular, square, and diamond piers is 12.5, 19.4 and 14.1 cm or in the dimensionless form S/w_p= 1.25, 1.94 and 1.00, respectively.

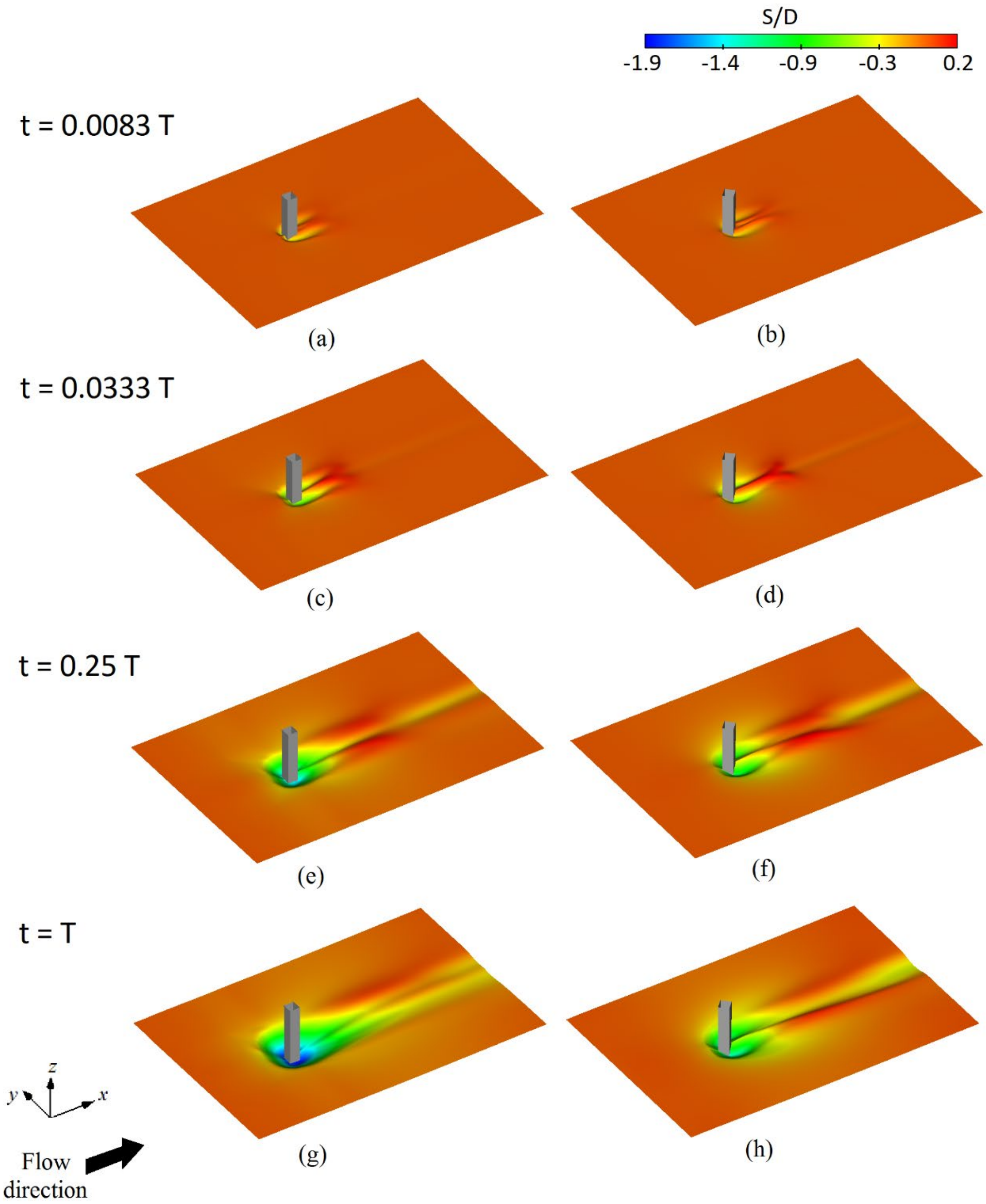

502

503 **Fig. 10** bed deformation at 4 different times of the simulation $t/T = 0.0083, 0.0333, 0.25, 1$ for the square and diamond

504 piers

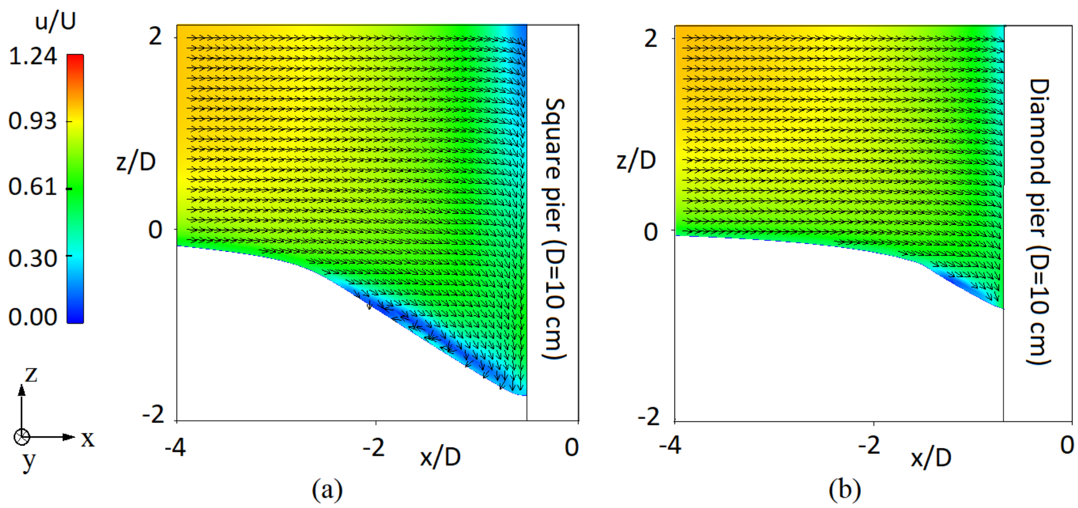

Fig. 11 instantaneous flow velocity vector field in symmetry plane (y=0) for (a) the square and (b) diamond piers

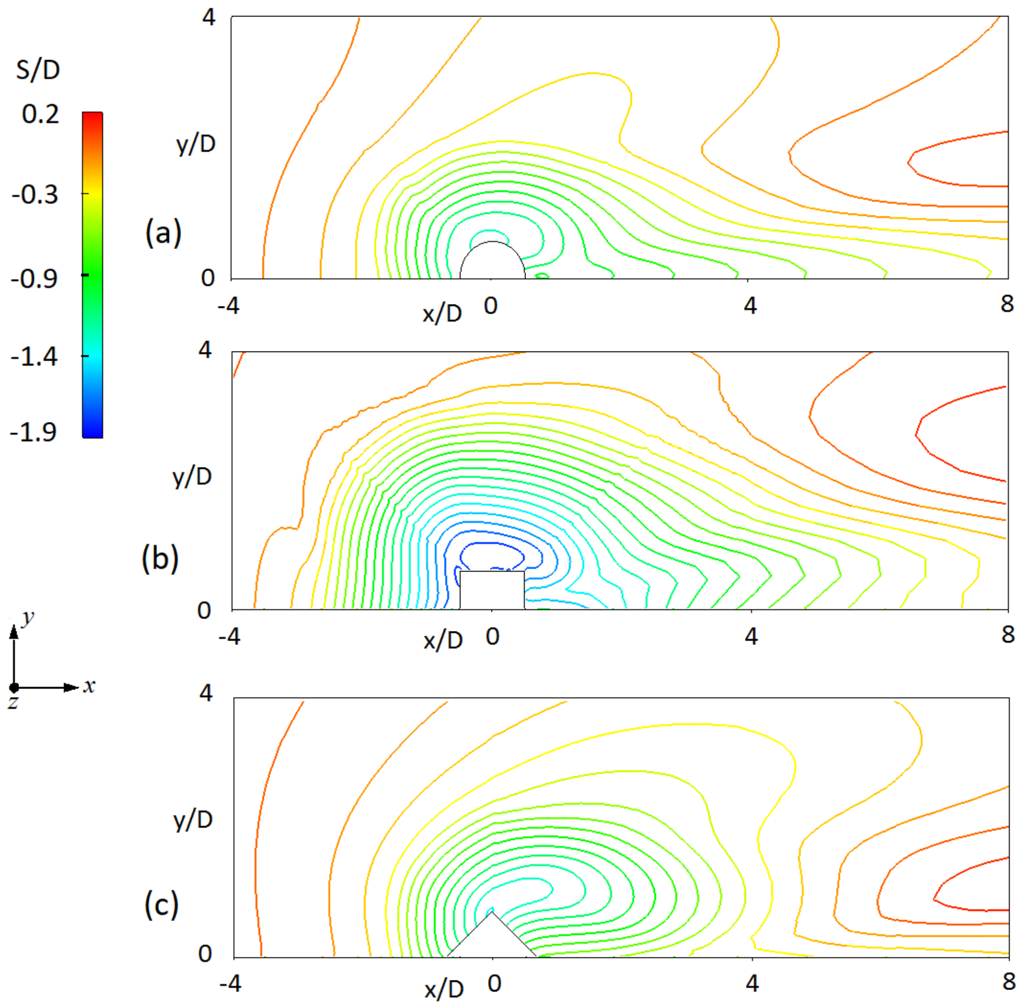

Fig. 12 bed displacement contour around the (a) circular, (b) square and (c) diamond pier in

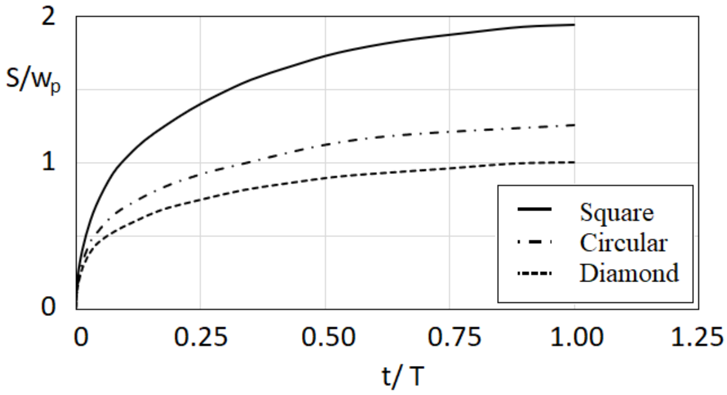

Fig. 13 changes in scour depth in time for circular, square and diamond piers

The simulation outcomes for the square and diamond piers are compared with the measurement results of Sumer et al. (1993) and Yao et al. (2018) in terms of normalized equilibrium scour depth S_{eq}/w_p. Sumer et al. (1993) concluded that the equilibrium scour depth in case of steady-current flow and live-bed conditions is only dependent on the pier shape and suggested a constant value of S_{eq}/w_p= 2 for both square and diamond piers. In a more recent study, Yao et al. (2018) investigated the local scour around submerged piers in live-bed conditions. From their results, S_{eq}/w_p was estimated around 2 and 1.5 for square and diamond piers, respectively. The calculated S_{eq}/w_p from the present simulation has a good agreement with the experimental data for the square piers, while the result for the diamond piers varies from the values reported in these studies. This difference can be justified from different aspects. Although the accuracy of the numerical model can be a matter of concern, the difference between the outcomes of the experimental investigations can also reveal that the impact of other factors, such as bed material gradation, Froude number, Shields parameter as well as flow depth need to be examined alongside the pier geometry. Therefore, more studies are needed to appreciate more clearly the precise role of different factors on scouring under live-bed conditions.

5 Conclusions

In this paper, the effect of the pier cross-section geometry on the flow behaviour and local scour in live-bed conditions was numerically investigated for a square-shaped pier with 90° (square pier) and 45° (diamond pier) orientation angles to the flow. For this purpose, a coupled hydro-morphodynamic model was developed in the OpenFOAM framework. The model was validated against flow and scour experimental data sets from various published studies. The simulation of flow behaviour around square and diamond piers showed that different flow mechanisms are responsible for the scour development around piers with respect to the orientation angle. In the case of the square pier, the formation of strong horseshoe vortices upstream of the piers is dominant, while it is very small and feeble in the case of the diamond pier. The scour simulation results revealed a faster rate of increase in scour depth around the square pier than the diamond and circular piers, which led to a deeper equilibrium scour hole. The simulation results presented a good agreement with the experimental data from the literature in terms of normalized equilibrium scour depth for the case of the square pier. It was discovered that the impact of other factors, such as bed material gradation, Froude number, Shields parameter, as well as flow depth, can be as important as the shape factor in the study of equilibrium scour depth in live-bed conditions.

6 References

ABBASNIA, A. H. & GHIASSI, R. 2011. Improvements on bed-shear stress formulation for pier scour computation. *International journal for numerical methods in fluids,* 67**,** 383-402.

AKHLAGHI, E., BABARSAD, M. S., DERIKVAND, E. & ABEDINI, M. 2020. Assessment the Effects of Different Parameters to Rate Scour around Single Piers and Pile Groups: A Review. *J Archives of Computational Methods in Engineering,* 27**,** 183-197.

AL-SHUKUR, A.-H. K., OBEID, Z. H. J. I. J. O. C. E. & TECHNOLOGY 2016. Experimental study of bridge pier shape to minimize local scour. 7**,** 162-171.

BAYKAL, C., SUMER, B. M., FUHRMAN, D. R., JACOBSEN, N. G. & FREDSØE, J. 2017. Numerical simulation of scour and backfilling processes around a circular pile in waves. *Coastal Engineering,* 122**,** 87-107.

BORDBAR, A., SHARIFI, S. & HEMIDA, H. 2021. Numerical Investigation of Different Sand Sliding Methods for Morphodynamic Modelling of scour around offshore structures. *Maritime Engineering (ICE)*.

CEBECI, T. & BRADSHAW, P. 1977. Momentum transfer in boundary layers. *Washington, DC, Hemisphere Publishing Corp.; New York, McGraw-Hill Book Co., 1977. 407 p.*

DARGAHI, B. 1987. Flow field and local scouring around a pier. *Bulletin No. TRITA-VBI,* 137.

DIAB, R., LINK, O. & ZANKE, U. 2010. Geometry of developing and equilibrium scour holes at bridge piers in gravel. *Canadian Journal of Civil Engineering,* 37**,** 544-552.

DRIEST, E. R. V. 1956. On turbulent flow near a wall. *Journal of the aeronautical sciences,* 23**,** 1007-1011.

ENGELUND, F. & FREDSØE, J. 1976. A sediment transport model for straight alluvial channels. *Hydrology Research,* 7**,** 293-306.

EXNER, F. M. 1925. Uber die wechselwirkung zwischen wasser und geschiebe in flussen. *Akad. Wiss. Wien Math. Naturwiss. Klasse,* 134**,** 165-204.

FERZIGER, J. H. & PERIC, M. 2008. *Numerische Strömungsmechanik*, Springer-Verlag.

FLEMING, J. L., SIMPSON, R., COWLING, J. & DEVENPORT, W. 1993. An experimental study of a turbulent wing-body junction and wake flow. *Experiments in fluids,* 14**,** 366-378.

GHIASSI, R. & ABBASNIA, A. H. 2013. Investigation of vorticity effects on local scouring. *J Arabian Journal for Science*

Engineering, 38**,** 537-548.

GOTHEL, O. 2008. Numerical modeling of flow and wave-induced scour around vertical structures.

HJORTH, P. 1975. *Studies on the nature of local scour*, Inst. för Teknisk Vattenresurslära, Lunds Tekniska Högskola, Lunds Univ.

HUNT, J. C. R., WRAY, A. A. & MOIN, P. 1988. Eddies, streams, and convergence zones in turbulent flows.

ISMAEL, A., GUNAL, M. & HUSSEIN, H. 2015. Effect of bridge pier position on scour reduction according to flow direction. *Arabian Journal for Science and Engineering,* 40**,** 1579-1590.

JACOBSEN, N. G. J. I. J. F. N. M. I. F. 2015. Mass conservation in computational morphodynamics: uniform sediment and infinite availability. 78**,** 233-256.

KHOSRONEJAD, A., KANG, S., BORAZJANI, I. & SOTIROPOULOS, F. 2011. Curvilinear immersed boundary method for simulating coupled flow and bed morphodynamic interactions due to sediment transport phenomena. *Advances in water resources,* 34**,** 829-843.

KHOSRONEJAD, A., KANG, S. & SOTIROPOULOS, F. 2012. Experimental and computational investigation of local scour around bridge piers. *Advances in Water Resources,* 37**,** 73-85.

KIM, H. S., ROH, M. & NABI, M. 2017. Computational modeling of flow and scour around two cylinders in staggered array. *J Water,* 9**,** 654.

KOLÁŘ, V. 2007. Vortex identification: New requirements and limitations. *International journal of heat and fluid flow,* 28**,** 638-652.

LIANG, D. & CHENG, L. 2005. Numerical model for wave-induced scour below a submarine pipeline. *Journal of waterway, port, coastal, and ocean engineering,* 131**,** 193-202.

LIU, X. & GARCÍA, M. H. 2008. Three-dimensional numerical model with free water surface and mesh deformation for local sediment scour. *Journal of waterway, port, coastal, and ocean engineering,* 134**,** 203-217.

MAHMOUD, A. H. J. L. S. J. 2020. Effect of soil particle size in reducing the Scour around bridge Piers at the Curved Channels. 17.

MELVILLE, B. W. 1975. *Local scour at bridge sites.* researchspace@ auckland.

MENDOZA-CABRALES, C. Computation of flow past a cylinder mounted on a flat plate. Hydraulic Engineering, 1993. ASCE, 899-904.

MENTER, F. R. 1992. Improved two-equation k–ω turbulence models for aerodynamic flows. NASA STI. Recon Technical Report 93, 22809.

MIR, B. H., LONE, M. A., BHAT, J. A., RATHER, N. A. J. G. & ENGINEERING, G. 2018. Effect of gradation of bed material on local scour depth. 36**,** 2505-2516.

MIR, B. H., LONE, M. A., RATHER, N. A. J. I. J. O. S. & TECHNOLOGY, T. O. C. E. 2019. Significance of shape factor of obstacle on local scour. 43**,** 323-330.

MIYAB, N. M., ESLAMIAN, S., DALEZIOS, N. R. J. H. O. D., IMPACTS, W. S. E., DROUGHT, A. O. & SCARCITY, W. 2017. River sediment in low flow condition.

NAGEL, T., CHAUCHAT, J., BONAMY, C., LIU, X., CHENG, Z. & HSU, T.-J. J. A. I. W. R. 2020. Three-dimensional scour simulations with a two-phase flow model. 103544.

NAJAFZADEH, M., BARANI, G.-A., AZAMATHULLA, H. M. J. N. C. & APPLICATIONS 2014. Prediction of pipeline scour depth in clear-water and live-bed conditions using group method of data handling. 24**,** 629-635.

OMARA, H., ABDEELAAL, G., NADAOKA, K., TAWFIK, A. J. M. G. & GEOTECHNOLOGY 2020. Developing empirical formulas for assessing the scour of vertical and inclined piers. 38**,** 133-143.

OMARA, H., ELSAYED, S., ABDEELAAL, G., ABD-ELHAMID, H. & TAWFIK, A. 2019. Hydromorphological numerical model of the local scour process around bridge piers. *Arabian Journal for Science and Engineering,* 44**,** 4183-4199.

PAN, J., HE, Z., SHIH, W. & CHENG, N. J. I. J. O. S. R. 2020. Numerical modeling of scour and deposition around permeable cylindrical structures.

PANDEY, M., AZAMATHULLA, H. M., CHAUDHURI, S., PU, J. H. & POURSHAHBAZ, H. 2020. Reduction of time-dependent scour around piers using collars. *Ocean Engineering,* 213**,** 107692.

QI, W. G., LI, Y. X., XU, K. & GAO, F. P. 2019. Physical modelling of local scour at twin piles under combined waves and current. *J Coastal Engineering,* 143**,** 63-75.

RIJN, L. C. V. 1984a. Sediment transport, part I: bed load transport *Journal of hydraulic engineering,* 110:1431-1456.

RIJN, L. C. V. 1984b. Sediment transport, part II: suspended load transport. *Journal of hydraulic engineering,* 110**,** 1613-1641.

ROULUND, A., SUMER, B. M., FREDSØE, J. & MICHELSEN, J. 2005. Numerical and experimental investigation of flow and scour around a circular pile. *Journal of Fluid Mechanics,* 534**,** 351-401.

SALAHELDIN, T. M., IMRAN, J. & CHAUDHRY, M. H. 2004. Numerical modeling of three-dimensional flow field around circular piers. *Journal of Hydraulic Engineering,* 130**,** 91-100.

SCHENDEL, A., HILDEBRANDT, A., GOSEBERG, N. & SCHLURMANN, T. 2018. Processes and evolution of scour around a monopile induced by tidal currents. *Coastal Engineering,* 139**,** 65-84

SOULSBY, R. 1997. *Dynamics of marine sands: a manual for practical applications*, Thomas Telford.

SOULSBY, R. & WHITEHOUSE, R. Threshold of sediment motion in coastal environments. Pacific Coasts and Ports' 97: Proceedings of the 13th Australasian Coastal and Ocean Engineering Conference and the 6th Australasian Port and Harbour Conference; Volume 1, 1997. Centre for Advanced Engineering, University of Canterbury, 145.

STAHLMANN, A. 2013. *Experimental and numerical modeling of scour at offshore wind turbines.* Hannover: Gottfried Wilhelm Leibniz Universität Hannover.

STAHLMANN, A. & SCHLURMANN, T. Numerical and Experimental Modeling of Scour at Tripod Foundations for Offshore Wind Turbines. 2012 2012 Paris, France. Proc of the 6th International Conference on Scour and Erosion, .

SUMER, B. M. 2002. *The mechanics of scour in the marine environment*, World Scientific.

SUMER, B. M., CHRISTIANSEN, N. & FREDSØE, J. 1993. Influence of cross section on wave scour around piles. *Journal of waterway, port, coastal, and ocean engineering,* 119**,** 477-495.

VAGHEFI, M., MOTLAGH, M. J. T. N., HASHEMI, S. S. & MORADI, S. 2018. Experimental study of bed topography variations due to placement of a triad series of vertical piers at different positions in a 180 bend. *J Arabian Journal of Geosciences,* 11**,** 102.

WANG, S., YANG, S., HE, Z., LI, L. AND XIA, Y. 2020. Effect of Inclination Angles on the Local Scour around a Submerged Cylinder. *Water resources research,* 12(10)**,** p.2687.

WARNER, J. C., SHERWOOD, C. R., SIGNELL, R. P., HARRIS, C. K. & ARANGO, H. G. 2008. Development of a three-dimensional, regional, coupled wave, current, and sediment-transport model. *Computers & Geosciences,* 34**,** 1284-1306.

YAGCI, O., YILDIRIM, I., CELIK, M. F., KITSIKOUDIS, V., DURAN, Z. & KIRCA, V. O. J. A. O. R. 2017. Clear water scour around a finite array of cylinders. 68**,** 114-129.

YAO, W., AN, H., DRAPER, S., CHENG, L. & HARRIS, J. M. J. C. E. 2018. Experimental investigation of local scour around submerged piles in steady current. 142**,** 27-41.

ZHANG, Q., ZHOU, X. L. & WANG, J. H. 2017. Numerical investigation of local scour around three adjacent piles with different arrangements under current. *J Ocean Engineering,* 142**,** 625-638.